Eur. Phys. J. A **19**, 89–104 (2004)
DOI 10.1140/epja/i2003-10103-6

THE EUROPEAN PHYSICAL JOURNAL A

Formation of heavy and superheavy elements by reactions with massive nuclei

G. Fazio[1], G. Giardina[1,a], A. Lamberto[1], R. Ruggeri[1], C. Saccà[2], R. Palamara[3], A.I. Muminov[4], A.K. Nasirov[4,5], U.T. Yakhshiev[6], F. Hanappe[7], T. Materna[7], and L. Stuttgé[8]

[1] INFN, Sezione di Catania, and Dipartimento di Fisica dell'Università di Messina, Messina, Italy
[2] Dipartimento di Scienze della Terra dell'Università di Messina, Messina, Italy
[3] Dipartimento PAU dell'Università di Reggio Calabria, Reggio Calabria, Italy
[4] Heavy Ion Physics Department, INP, Tashkent, Uzbekistan
[5] Bogoliubov Laboratory of the Theoretical Physics, JINR, Dubna, Russia
[6] Theoretical Physics Department, National University of Uzbekistan, Tashkent, Uzbekistan
[7] Université Libre de Bruxelles, Bruxelles, Belgium
[8] Institut de Recherches Subatomiques, Strasbourg, France

Received: 22 April 2003 / Revised version: 26 June 2003 /

Communicated by D. Guerreau

Abstract. The effects of the entrance channel and shell structure on the experimental evaporation residues have been studied by analyzing the ^{32}S + ^{182}W, ^{48}Ti + ^{166}Er and ^{60}Ni + ^{154}Sm reactions leading to ^{214}Th*; the ^{40}Ar + ^{181}Ta reaction leading to ^{221}Pa*; the ^{48}Ca + ^{243}Am, ^{248}Cm, ^{249}Cf reactions leading to the ^{291}115, ^{296}116 and ^{297}118 superheavy compound nuclei, respectively. The fusion mechanism and the formation of evaporation residues of heavy and superheavy nuclei have been studied. In calculations of the excitation functions for capture, fusion and evaporation residues we used such characteristics as mass asymmetry of nuclei in the entrance channel, binding energies and shape of colliding nuclei, potential energy surface, driving potential, partial-fusion cross-sections and survival probability of the compound nucleus, $\Gamma_\mathrm{n}/\Gamma_\mathrm{f}$ ratio at each step along the de-excitation cascade of the compound nucleus. The calculations have allowed us to make useful conclusions about the mechanism of the fusion-fission process, which is in competition with the quasifission process, and the production of the evaporation residues.

PACS. 25.70.Gh Compound nucleus – 25.70.-z Low and intermediate energy heavy-ion reactions – 27.80.+w $190 \le A \le 219$ – 27.90.+b $A \ge 220$

1 Introduction

In this paper we analyze the importance of the entrance channel effect on the fusion-fission reaction mechanism in collisions of massive nuclei by comparing the excitation functions of evaporation residues (ER) measured for different mass asymmetry reactions. Often the excitation functions of evaporation residues, measured in various reactions leading to the same compound nucleus (CN), differ not only by the position of the maximum but also by the value of their maxima. The study of characteristics of nuclei and the fusion-fission process which are responsible for such a difference in the evaporation residue cross-sections is necessary for finding the optimal conditions for the synthesis of new superheavy elements. The difference in the measured evaporation residues for the reactions leading to the same compound nuclei can be explained by the difference in the excitation functions of the fusion and survival probability of the excited compound nucleus. A decrease in the fusion cross-sections is connected with an increase in the contribution of the quasifission process. Quasifission reactions are binary processes which exhibit some of the characteristics of fusion-fission events, such as the full relaxation of the relative kinetic energy and considerable transfer of mass between the two fragments. The basic difference between the fusion-fission and quasifission processes is that the compound-nucleus formation is not achieved in the latter mechanism. In quasifission reactions, a dinuclear system, which is formed at the capture stage of heavy-ion collisions, can evolve over the potential energy surface before reaching mass symmetry or decay by way of overcoming the quasifission barrier. The latter decreases usually with an increase in the mass symmetry. Quasifission can be thought of as a bridge between deep inelastic scattering (in which the relative kinetic energy

---

[a] e-mail: `giardina@nucleo.unime.it`

can be fully damped, but mass asymmetry of the entrance channel is mostly preserved) and compound-nucleus fission reactions, in which all the information on the entrance channel is lost [1–11].

A dinuclear system concept (DNS) [12] reveals the reason for the strong decrease in the fusion cross-section for a massive system or for a more symmetric entrance channel. It allows us to estimate the decrease in the fusion probability due to an increase in the quasifission process.

Calculations based on the DNS concept show [13,14] that entrance channel effects are important for the description of the experimental data in the case of collisions of massive nuclei.

In the present work, we consider a set of the experimental data on the production of ER in the reactions with different mass asymmetries leading to the same ^{214}Th* CN. We also compare our calculation results with the experimental data on reactions leading to the ^{221}Pa* CN. The capture, fusion and ER cross-sections for the ^{48}Ca + ^{243}Am, ^{48}Ca + ^{248}Cm and ^{48}Ca + ^{249}Cf reactions leading to the ^{291}115, ^{296}116 and ^{297}118 superheavy elements, respectively, have been calculated.

The aim of this paper is to analyze the effect of the intrinsic fusion and quasifission barriers on the distribution of the partial-fusion cross-sections which reveals the competition between complete fusion and quasifission. The partial capture cross-sections are calculated by solving the equation of motion for the relative distance and orbital angular momentum, taking into account dissipation of the collective kinetic energy [13,14]. The maximum value of the orbital angular momentum up to which the capture can occur (at a given beam energy) is calculated dynamically. The partial-fusion cross-sections are calculated from the capture cross-sections taking into account the competition between complete-fusion and quasifission processes. This competition is determined by the factor P_{CN} which is calculated statistically, using intrinsic fusion and quasifission barriers.

The composition of the paper is as follows. Basic features of the dynamical approach and the advanced statistical model are described in sect. 2. In sect. 3, we compare the results of our calculations with the available experimental data and discuss the effect of the entrance channel on the formation of the evaporation residue for the reactions leading to compound nuclei ^{214}Th* and ^{221}Pa*. The calculated excitation functions for the capture, fusion and evaporation residue formation for the ^{48}Ca + (^{243}Am, ^{248}Cm, ^{249}Cf) reactions leading to the ^{291}115, ^{296}116 and ^{297}118 superheavy compound nuclei, respectively, are presented in sect. 4. Conclusions are presented in sect. 5.

2 Capture, fusion and evaporation residue cross-sections in the dinuclear system concept

According to the DNS concept [12], the fusion between heavy ions is a complete transfer of all the nucleons of a light nucleus to a heavy one and formation of a compound nucleus compact in shape. Fusion of nuclei is considered as a two-stage process. The first step is the capture, *i.e.* the overcoming of the Coulomb barrier by the nuclei moving along the axis connecting nuclear centers, followed by a formation of a nuclear composite system (the so-called dinuclear system) [15]). The second step is the transformation of the DNS (mononucleus) into a compact compound nucleus via a multinucleon transfer, the overlapping of nucleon distributions of nuclei being small. Due to the great value of the inertia parameter of deformation, the change in the nuclear shape is not so big and the area of the overlapping between the nuclei remains small: it is about 5-6% of the total volume. The shell structure of interacting nuclei is retained during the multinucleon transfer. During this transformation, the system should overcome the intrinsic fusion barrier (B^*_{fus}) on the potential energy surface moving in the direction of the mass (charge) asymmetry axis. For light and intermediate nuclear systems or for heavy nuclear systems with a larger mass asymmetry, the intrinsic fusion barrier is equal to zero and the capture immediately leads to fusion. Therefore, in those cases, the fusion cross-section is calculated in the framework of well-known models [16]. The appearance of hindrance in the compound-nucleus formation in reactions with massive nuclei or in symmetric heavy-ion reactions was recognized earlier in the framework of the macroscopic dynamic models (see [17,18] for references). According to this type of models, the extra-extra push energy E_{xx} is needed to satisfy a necessary condition for forming a compound nucleus in heavy-ion reactions. For heavier nuclear systems and/or for a high angular momentum, the beam energy in the CM system must exceed the maximum in the one-dimensional interaction barrier by the amount E_{xx} in order to form the compound nucleus. This additional energy is connected with the shape of the mononucleus formed at capture and depends on mass and charge numbers of initial nuclei. In the DNS concept, B^*_{fus} is connected by mass (charge) asymmetry degrees of freedom of a dinuclear system and it is determined by the potential energy surface. It is built as a sum of binding energies of fragments and the nucleus-nucleus potential, subtracting the sum of the compound-nucleus binding energy and its rotational energy. Therefore, it is a function of the charge $Z = Z_1$ of one of the fragments ($Z_2 = Z_{\mathrm{tot}} - Z$, Z_{tot} is the total charge number of the system) forming the DNS and the relative distance between their centers R (see eq. (1)). In the case of the interaction of deformed nuclei, the nucleus-nucleus potential depends on their orientations:

$$\begin{aligned} U(A,Z,;R,\ell,\beta_1,\alpha_1;\beta_2,\alpha_2) = {} & B_1 + B_2 \\ & + V(Z,\ell,\beta_1,\alpha_1;\beta_2,\alpha_2;R) \\ & - (B_{\mathrm{CN}} + V_{\mathrm{CN}}(\ell)). \qquad (1) \end{aligned}$$

Here, B_1, B_2 and B_{CN} are the binding energies of the nuclei in a DNS and of the CN, respectively, which were obtained from [19,20]; V is the nucleus-nucleus interaction potential including the Coulomb, nuclear and rotational parts; β_i are the fragment deformation parameters and α_i are the orientations in respect to the beam direction (see appendix A); $V_{\mathrm{CN}}(\ell)$ is the rotational energy of the

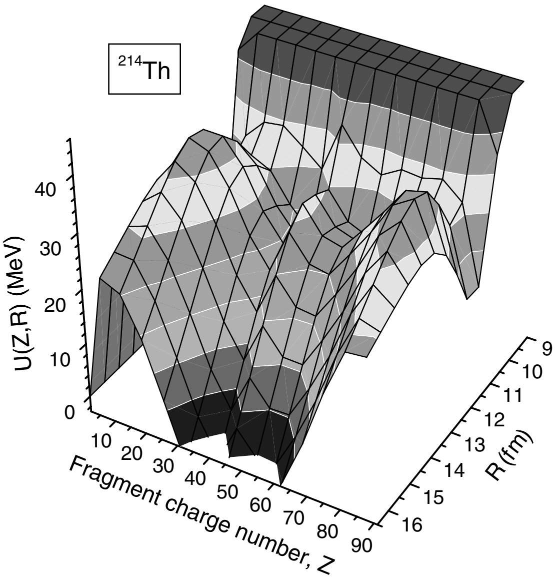

Fig. 1. Potential energy surface $U(A, Z; R; \ell = 0)$ for dinuclear systems leading to the compound nucleus ^{214}Th as a function of the charge number Z of one of its fragments and a relative distance between centers of nuclei.

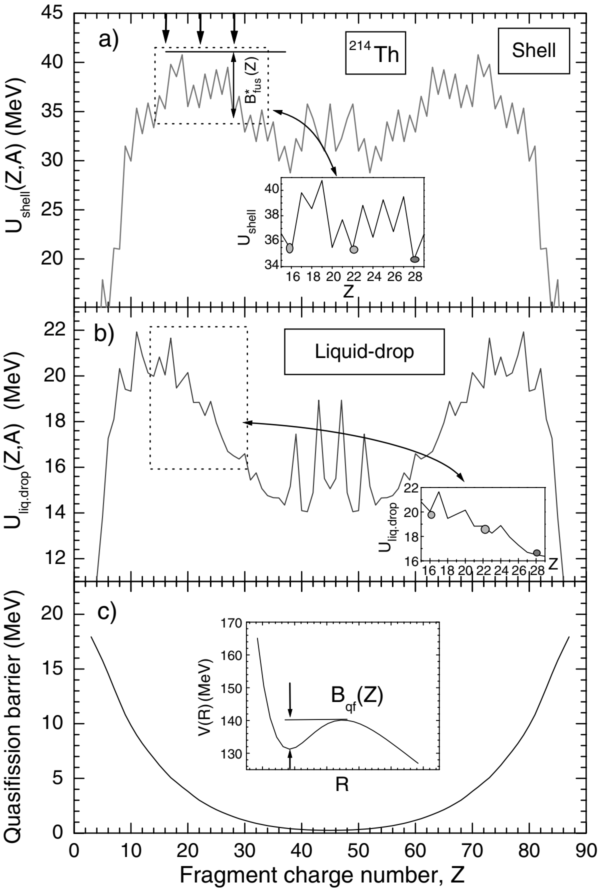

Fig. 2. Driving potential $U(Z, A, R_{\mathrm{m}}; \ell = 0)$ as a function of the charge number Z of a DNS fragment calculated by (1) using binding energies from the nuclear data in [19] (a) and those obtained with the liquid-drop model (b). The vertical arrows indicate the initial charge number of light nuclei in the ^{32}S + ^{182}W, ^{48}Ti + ^{166}Er and ^{60}Ni + ^{154}Sm reactions leading to ^{214}Th. Panel (a) shows the intrinsic fusion B^*_{fus} for the ^{60}Ni + ^{154}Sm reaction only. In panel (c), the quasifission barriers B_{qf} are shown as a function of the charge number of a DNS fragment.

compound nucleus. The distribution of neutrons between two fragments of the given proton numbers Z_1 and Z_2 (or the ratios A_1/Z_1 and A_2/Z_2 for both fragments) was determined by minimizing the potential $U(A_1, Z_1; R)$ as a function of A_1 for each Z_1. The potential energy surface $U(A, Z; R; \ell = 0)$ presented in fig. 1 was calculated for the reactions leading to the ^{214}Th CN with the orientations of reacting nuclei $\alpha_1 = 60°$ and $\alpha_2 = 15°$. It is convenient to calculate the competition between complete fusion and quasifission proceeding from the driving potential. The latter is extracted from the potential energy surface $U(A, Z; R; \ell)$ considering it as a function of mass $A = A_1$ ($A_2 = A_{\mathrm{tot}} - A$) and charge $Z = Z_1$ of one of the fragments forming the DNS at the value $V(R)$ (see appendix A) of the internuclear distance $R_{\mathrm{m}}(Z)$ corresponding to the minimum of the nucleus-nucleus potential (bottom of the pocket) for a given fragment Z; A_{tot} is the mass of the compound nucleus.

B^*_{fus} is determined by the difference between the maximum value of the driving potential $U(Z, A, R_{\mathrm{m}})$ and its value at the point corresponding to the initial charge asymmetry of the considered reaction (fig. 2). If the excitation energy of the dinuclear system $E^*_{\mathrm{DNS}} = E_{\mathrm{c.m.}} - V(R_{\mathrm{m}}, \ell))$ is not enough for overcoming B^*_{fus}, the dinuclear system decays into two fragments and undergoes quasifission after nucleon exchange between its components. The quasifission occurs due to motion along the relative internuclear distance R and depends on the $V(R)$ nucleus-nucleus interaction potential. At capture, the DNS is in the potential well (fig. 2, bottom). Thus, for quasifission, it is necessary to overcome the barrier B_{qf} which is equal to the depth $V(R)$ of the well. If the DNS excitation energy is not enough for overcoming B_{qf}, it fluctuates on charge asymmetry moving to a more symmetric configuration forming a super-deformed mononucleus. A DNS can decay into two fragments due to a decrease in B_{qf} with decreasing the charge asymmetry. The driving potential containing these characteristics under discussion is significant for considering the fusion process as a motion of a system along the mass (charge) asymmetry degree of freedom. The capture and fusion cross-sections are calculated for different orientations and the obtained results are averaged.

In the DNS concept [12], the evaporation residue cross-section is factorized as follows:

$$\sigma_{\mathrm{er}}(E) = \sum_{\ell=0}^{\ell_d} (2\ell + 1)\sigma_\ell^{\mathrm{fus}}(E, \ell) W_{\mathrm{sur}}(E, \ell). \tag{2}$$

Here, the effects connected with the entrance channel are included in the partial-fusion cross-section $\sigma_\ell^{\mathrm{fus}}(E)$, which is defined by the expressions

$$\sigma_\ell^{\mathrm{fus}}(E) = \sigma_\ell^{\mathrm{capture}}(E) P_{\mathrm{CN}}(E,\ell), \tag{3}$$

$$\sigma_\ell^{\mathrm{capture}}(E) = \frac{\lambda^2}{4\pi}\mathcal{P}_\ell^{\mathrm{capture}}(E), \tag{4}$$

where λ is the de Broglie wavelength of the entrance channel, $P_{\mathrm{CN}}(E,\ell)$ is the factor taking into account the decrease in the fusion probability due to a break-up of the DNS (quasifission); $\mathcal{P}_\ell^{\mathrm{capture}}(E)$ is the capture probability which depends on the collision dynamics and is determined by the number of partial waves (ℓ_d) leading to capture.

2.1 Capture

The capture cross-section is determined by the number of partial waves which lead colliding nuclei into a trap in the well of the nucleus-nucleus potential. The number of the partial waves ℓ_d was obtained by solving classical equations of motion for the relative distance and orbital angular momentum taking into account dissipation of the collective kinetic energy [13,14]:

$$\frac{\mathrm{d}(\mu(R)\,\dot{R})}{\mathrm{d}t} + \gamma_R(R)\,\dot{R}(t) = F(R), \tag{5}$$

$$F(R) = -\frac{\partial V(R)}{\partial R} - \dot{R}^2 \frac{\partial \mu(R)}{\partial R}, \tag{6}$$

$$\frac{\mathrm{d}L}{\mathrm{d}t} = \gamma_\theta(R) R(t) \left(\dot{\theta} R(t) - \dot{\theta}_1 R_{1\mathrm{eff}} - \dot{\theta}_2 R_{2\mathrm{eff}}\right), \tag{7}$$

$$L_0 = J_R \dot{\theta} + J_1 \dot{\theta}_1 + J_2 \dot{\theta}_2, \tag{8}$$

$$E_{\mathrm{rot}} = \frac{J_R \dot{\theta}^2}{2} + \frac{J_1 \dot{\theta}_1^{\,2}}{2} + \frac{J_2 \dot{\theta}_2^{\,2}}{2}, \tag{9}$$

where $R \equiv R(t)$ is the relative motion coordinate; $\dot{R}(t)$ is the corresponding velocity; L_0 and E_{rot} are determined by initial conditions; J_R and $\dot{\theta}$, J_1 and $\dot{\theta}_1$, J_2 and $\dot{\theta}_2$ are the moment of inertia and angular velocities of the DNS and its fragments, respectively (J_R, J_1 and J_2 are determined in appendix A); γ_R and γ_θ are the friction coefficients for the relative motion along R and the tangential motion when two nuclei roll onto each other's surfaces, respectively; $V(R)$ is the nucleus-nucleus potential which includes Coulomb, nuclear and rotational energies (see eq. (A.1) in appendix A); $\mu(R,t))$ is the reduced mass of the system:

$$\mu(R,t) = \tilde{\mu}(R,t) + \delta\mu(R,t), \tag{10}$$

where

$$\tilde{\mu}(R,t) = m_0 A_{\mathrm{T}}(R,t) \cdot A_{\mathrm{P}}(R,t)/(A_{\mathrm{T}}(R,t) + A_{\mathrm{P}}(R,t))$$

at $t = 0$ and $A_{\mathrm{T}}(R)$ and $A_{\mathrm{P}}(R)$ are equal to mass numbers of the target and projectile nucleus, respectively; m_0 is the nucleon mass. The time dependences of $A_{\mathrm{P}}(t) = Z_{\mathrm{P}}(t) + N_{\mathrm{P}}(t)$ and $A_{\mathrm{T}}(t) = Z_{\mathrm{T}}(t) + N_{\mathrm{T}}(t)$ are found by solving the master equation for the evolution of occupation numbers of single-particle states in nuclei as in [21]; $\delta\mu(R,t)$ is the change of μ during the interaction due to nucleon exchange and overlapping of nucleon densities of interacting nuclei (see appendix A);

$$R_{1(2)\mathrm{eff}} = \frac{R_{01(02)}}{R_{01} + R_{02}} R\,,$$

where $R_{01(02)}$ is the nucleus equilibrium radius: $R_{0i} = r_0 A_i^{1/3}, r_0 = 1.18$ fm.

In the presented calculation, the changes in the nucleus-nucleus potential and reduced mass due to the nucleon exchange and the change in the overlapping of nucleon densities have been taken into account (see appendix A). Note that the estimation showed that $\delta V(R)$ and $\delta\mu(R)$ were small at the distance corresponding to the capture. These quantities and the nucleus-nucleus potential $V(R)$ depend on mutual orientations of symmetry axes of the deformed nuclei with relation to $R(t)$. The contribution of these quantities increases after the capture stage while the system is in the potential well and the nuclei still rotate coming to sticking. Moreover, contributions of $\dot{R}\,\mathrm{d}\mu(R(t))/\mathrm{d}t$ and $\dot{R}^2\mathrm{d}(\mu(R(t))/\mathrm{d}R$ in eqs. (5) and (6) are negligible. Therefore, these terms do not affect the calculated results for ℓ leading to the capture. For our calculations of the capture cross-sections it is only necessary to establish the fact that the dinuclear system has been trapped into the potential well at a given value of the projectile energy and initial orbital angular momentum. In this paper the fusion process is considered using a statistical method which will be discussed in the next section. The inertia moment of the orbital motion of a dinuclear system is changed by the distance between the centers of nuclei during interaction (rotation of nuclei around the axis perpendicular to the reaction plane while the system is in the potential well). This fact has been taken into account in the calculation of the capture stage. The change in the inertia moment of a dinuclear system due to the turning of (deformed) nuclei around their own axes (rolling) is small because during the capture stage the maximum values of turning angles of light and heavy nuclei around their own axes is about 20°–25° and 6°–7°, respectively. Therefore, the effect from the turning of nuclei around their own axes on the rotational energy is negligible.

The friction coefficients γ_R (γ_θ), *i.e.*, the change in the nucleus-nucleus potential and reduced mass of relative motion during the interaction time t, are calculated from the estimation of the coupling between the relative motion of nuclei and the intrinsic excitation of nuclei [22]. Therefore, the numerical calculation of eqs. (5), (6) and (7) for the relative motion and master equations for the occupation numbers (see [21]) of single-particle states were solved with the $\Delta t = 2 \cdot 10^{-23}$ s. During this time, the coefficients of equations for one degree of freedom are considered independent of the other degrees of freedom. After the Δt time, all the coefficients and matrix elements are calculated for the thus obtained values for the collective variables.

2.2 Fusion

The competition between fusion and quasifission is taken into account by the factor $P_{\mathrm{CN}}(E,\ell)$ (fusion factor, hereafter) which is calculated in the framework of the statistical model. This way was first used in [12]. Validity of using the statistical method is justified due to fact that in the quasifission process there is a full relaxation of the relative kinetic energy and mass (charge) asymmetry between the two fragments [11]. The statistical method is acceptable in the calculation of the competition between complete-fusion and quasifission processes due to the fact that thermal equilibrium is established in the DNS rather fast, for a few units of 10^{-22} s:

$$\tau_{\mathrm{ther}} = 2.6/T^2_{\mathrm{DNS}} \cdot 10^{-22}\,\mathrm{s}.$$

Here T_{DNS} is the effective temperature of a DNS: T_{DNS}, where $E^*_{\mathrm{DNS}} = E_{\mathrm{c.m.}} - V(Z,A,R_{\mathrm{m}})$ is the excitation energy of a DNS with the fragments (Z,A) and $(Z_{\mathrm{tot}} - Z, A_{\mathrm{tot}} - A)$; $E_{\mathrm{c.m.}}$ is the beam energy in the CM system and $V(R_{\mathrm{m}})$ is the minimum value of the nucleus-nucleus potential in the potential well.

Duration of the quasifission is longer than τ_{ther} by an order of magnitude. It is more than $5 \cdot 10^{-21}$ s which was estimated by the analysis of experimental data on the quasifission reactions [6,23–25]. The fusion time is longer than the quasifission reaction time. The calculation of mass and charge yields in the frame of a microscopic model showed that the time of formation of a DNS with a given mass (charge) asymmetry changed from $5 \cdot 10^{-21}$ s to $9 \cdot 10^{-20}$ s [26–28]. The study of the experimental data on the fusion-fission and quasifission reactions induced by ^{48}Ca and ^{58}Fe projectiles on ^{232}Th, ^{238}U, ^{248}Cm and ^{249}Cf targets [29,30] showed that mass and charge distributions could reach their equilibrium values even in quasifission reactions. It is clear from the fact that positions of maxima of the mass distribution of reaction products correspond to local minima of the DNS potential energy surface. The yields of quasifission products, which were calculated in the framework of the diffusion model based on the transfer master equation [31,32] indicate that the fragments resulted from the quasifission process can appear in the mass-symmetric region and mix with the fragments coming from the fusion-fission process. Experimentally, it is difficult to distinguish between fusion-fission and quasifission reaction products. Only analysis of correlation between reaction fragment mass and angular distributions allows us to estimate a ratio between contributions of quasifission and fusion-fission processes. These theoretical and experimental results on the quasifission justify the use of a statistical approach to the estimations of the competition between complete-fusion and quasifission processes. Calculations of complete fusion in competition with quasifission can be performed in the framework of statistical methods. The probability of the complete-fusion realization is related to the ratio of the level densities, depending on the intrinsic fusion or quasifission barriers, by the expression:

$$P_{\mathrm{CN}} = \frac{\rho(E^*_{\mathrm{DNS}} - B^*_{\mathrm{fus}})}{\rho(E^*_{\mathrm{DNS}} - B^*_{\mathrm{fus}}) + \rho(E^*_{\mathrm{DNS}} - B_{\mathrm{qf}})}, \qquad (11)$$

where $\rho(E^*_{\mathrm{DNS}} - B^*_K)$ is the level density for the DNS at the quasifission and intrinsic fusion barriers ($B_K = B_{\mathrm{qf}}, B^*_{\mathrm{fus}}$) (all details are in [14]). The final result for the partial-fusion cross-sections is obtained by averaging over the contributions of different mutual orientations of the symmetry axes of the reacting nuclei.

2.3 Survival probability

An advanced statistical model (ASM), described in detail in [33–35], allows us to take into account the dynamical aspects of the fission-evaporation competition during the evolution of the compound nucleus along the de-excitation cascade. The model accounts for the angular momentum and parity coupling; it allows for the neutron, proton, and α-particle multiple emission, as well as for the fission channel and full γ-cascade in the residual nuclei.

Particular attention is paid to the determination of level densities. These are calculated in the non-adiabatic approach allowing for rotational and vibrational enhancements. These collective effects are gradually removed above a certain energy E_{Cor}. Following [33], in the case of rotational enhancement, the E_{Cor} energy [36,37] is related to the Coriolis force which couples intrinsic and collective motions. The used level densities acquire a dynamical aspect through the dependence of the Coriolis force and of the rotational enhancement on the nuclear shape, which is, in turn, obtained from the classical model of a rotating liquid drop. Intrinsic level densities are calculated using the Ignatyuk approach [38], which takes into account shell structure effects and pairing correlations. The use of the correct level densities is of fundamental importance for the present analysis as they determine the phase space available for each channel, the very essence that governs statistical decay.

In the case of the evaporation residue production, one should also carefully consider the low-energy level densities since in this energy interval most of the evaporation residues is formed. That is why in our calculations we use the super-fluid model of the nucleus [39], with the standard value of pairing correction $\Delta = 12/\sqrt{A}$ MeV. The yrast lines are automatically included in our calculations by the requirement that the total excitation energy should be higher than the rotational energy, otherwise the level density is set to zero.

For the fission barriers, we use the predictions of the rotating droplet model (angular-momentum dependent) as parameterized by Sierk [40] and allow for the angular momentum and temperature fade-out of the shell corrections [34]. This is expressed by the formula for the actual fission barrier used in calculations:

$$B_{\mathrm{fis}}(J,T) = c\ B^m_{\mathrm{fis}}(J) - h(T)\ q(J)\ \delta W\,, \qquad (12)$$

which includes a dependence on temperature of the compound nucleus

$$h(T) = \begin{cases} 1, & T \leq 1.65\,\mathrm{MeV}, \\ k\exp(-mT), & T > 1.65\,\mathrm{MeV}, \end{cases}$$

and

$$q(J) = \{1 + \exp[(J - J_{1/2})/\Delta J]\}^{-1},$$

where $B^{m}_{\mathrm{fis}}(J)$ is the parameterized macroscopic fission barrier [40] depending on the angular momentum J, $\delta W = \delta W_{\mathrm{sad}} - \delta W_{\mathrm{gs}} \simeq -\delta W_{\mathrm{gs}}$ is the microscopic (shell) correction to the fission barrier taken from the tables [20] and the constants for the macroscopic fission barrier scaling, temperature, and angular-momentum dependences of the microscopic correction are chosen as follows: $c = 1.0$, $k = 5.809$, $m = 1.066\,\mathrm{MeV}^{-1}$, $J_{1/2} = 24\hbar$ for nuclei with $Z \simeq 80$–100 (or $J_{1/2} = 20\hbar$ for nuclei with $Z > 100$), and $\Delta J = 3\hbar$. This procedure allows the shell corrections to become dynamical quantities, too.

Dissipation effects, which delay fission, are treated according to [41,42]. These include Kramers' stationary limit [43] and an exponential factor applied to Kramers' fission width to account for the transient time, after which the statistical regime is reached. The systematics obtained by Bhattacharya *et al.* [44] allows us to take into account the dependences of the reduced dissipation coefficient β_{dis} on the incident energy per nucleon ϵ and compound-nucleus mass A. β_{dis} is the ratio between the friction coefficient γ, which describes the coupling of the fission degree of freedom to the intrinsic degrees of freedom, and the reduced mass of the system. This ratio characterizes the dissipative and diffusive motion.

In the calculation of the fission width including the Kramers' factor, we use for reduced dissipation coefficient expressed by a simple formula proposed by Bhattacharya *et al.* [44]:

$$\beta_{\mathrm{dis}}(\epsilon, A) = a\epsilon + bA^3, \tag{13}$$

where $a = 0.18$, $b = 0.357 \times 10^{-6}$. For the investigated reactions, the β_{dis} values range from about 6 to $7 \times 10^{21}\,\mathrm{s}^{-1}$.

In the present ASM calculations, the target-projectile fusion cross-section was determined by formula (3). The survival probability W_{sur} is defined by the partial-fusion cross-section which affects the fission barrier and the $\Gamma_{\mathrm{n}}/\Gamma_{\mathrm{f}}$ ratio which determines the evaporation residue production.

3 Comparison of DNS model results and experimental data

The qualitative difference between fusion excitation functions of reactions leading to the same compound nucleus allows us to analyze the effect of the shell structure on the fusion mechanism. Experimental excitation functions measured in the ^{32}S + ^{182}W, ^{48}Ti + ^{166}Er, and ^{60}Ni + ^{154}Sm reactions [11,45] for the ^{214}Th* CN, and in the ^{40}Ar + ^{181}Ta [46,47] reaction for the ^{221}Pa* CN have been compared with the results of calculation in the framework of the method presented in [13,14,33,34]. It is shown that the effect of the shell structure is revealed by comparing the calculated excitation functions of the fusion and evaporation cross-sections. To show the origin of these differences, the partial-fusion cross-sections against the beam energy values are presented.

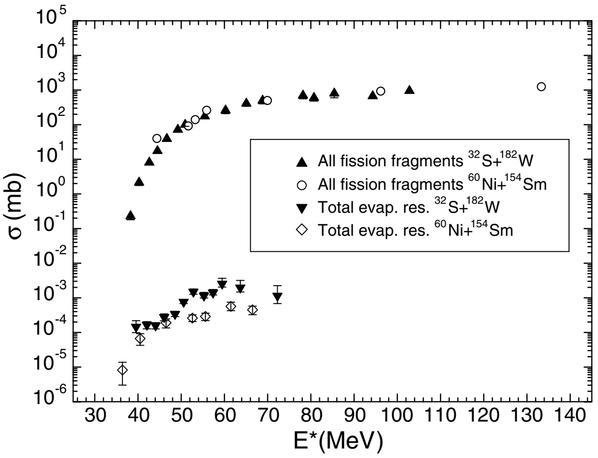

Fig. 3. The experimental data obtained from [11,45] *versus* the excitation energy of the compound nucleus E^* for the ^{32}S + ^{182}W, ^{48}Ti + ^{166}Er, and ^{60}Ni + ^{154}Sm reactions leading to the ^{214}Th* CN.

3.1 The reactions leading to ^{214}Th*

In this section we consider experimental results of the ^{32}S + ^{182}W, ^{48}Ti + ^{166}Er and ^{60}Ni + ^{154}Sm reactions [11, 45] (leading to the ^{214}Th* CN) and analyze the effect of the entrance channel on the formation of evaporation residues.

In fig. 3, the experimental results taken from [11,45] are presented *versus* the excitation energy E^* of the compound nucleus.

One can infer that at the same excitation energy E^* the capture cross-sections are almost equal. But the evaporation residue cross-sections of the ^{60}Ni + ^{154}Sm reaction deviate from those for the ^{32}S + ^{182}W reaction at $E^* > 50\,\mathrm{MeV}$. Such result may be connected with the dynamical effects of the entrance channel which are different for the considered reactions.

To analyze the role of the entrance channel, we compare the results of calculations (performed in framework of the above-presented method) of the capture, fusion and evaporation residue cross-sections for the ^{32}S + ^{182}W (I) reaction (fig. 4a), the ^{48}Ti + ^{166}Er (II) reaction (fig. 4b) and for the ^{60}Ni + ^{154}Sm (III) reaction (fig. 4c), leading to the same ^{214}Th* CN. Some parameters in the entrance channel are presented in table 1. The value of the charge asymmetry parameter $\eta_Z = (Z_2 - Z_1)/(Z_1 + Z_2)$ changes from 0.644 (for the more asymmetric reaction (I)) to 0.511 (for the reaction (II)), and to 0.378 (for the more symmetric reaction (III)).

The fusion barrier is very low and the quasifission barrier is high in the case of the reaction (I) induced by the

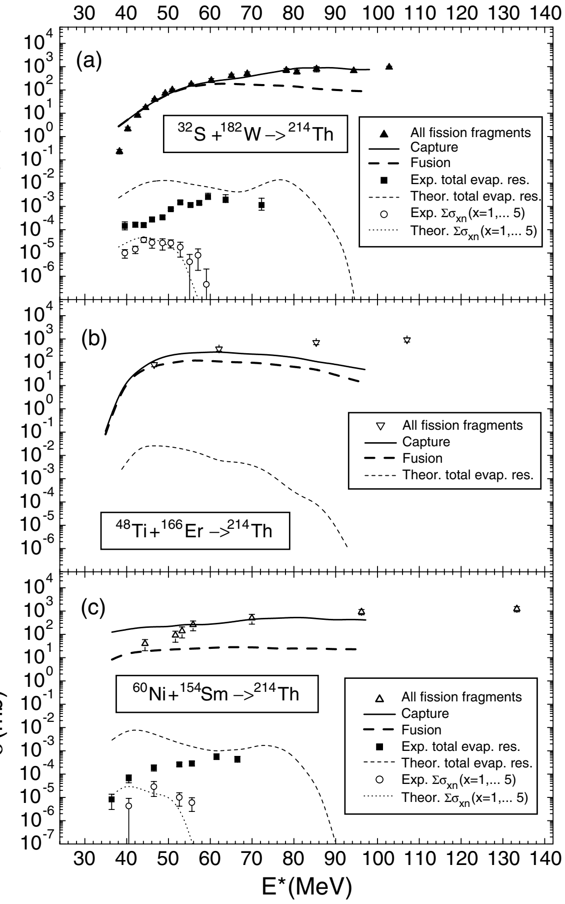

Fig. 4. The calculated capture, fusion and evaporation residue cross-sections for the ^{32}S + ^{182}W (a), ^{48}Ti + ^{166}Er (b), and ^{60}Ni + ^{154}Sm (c) reactions are compared with the experimental data on the fission of the compound nucleus and evaporation residue formations from [11,45] which were already presented in fig. 3.

Table 1. Charge asymmetry, intrinsic fusion and quasifission barriers (B^*_{fus}) and (B_{qf}), and fusion factor (P_{CN}) for the reactions leading to the ^{214}Th* CN.

Reactions	η_Z	B^*_{fus} (MeV)	B_{qf} (MeV)	P_{CN}
^{32}S + ^{182}W (I)	0.644	1.3	5.63	0.868
^{48}Ti + ^{166}Er (II)	0.511	5.39	3.01	0.201
^{60}Ni + ^{154}Sm (III)	0.378	6.25	1.50	0.103

^{32}S beam when realistic binding energies of the interacting DNS nuclei are used in calculations (see the top panel of fig. 2). The first arrow marks a point at the left-hand side of the maximum of the driving potential curve, and there is a small barrier equal to 1.3 MeV on the way to fusion only due to the odd-even effect. If one considers the driving potential calculated in the liquid-drop model (see the middle panel of fig. 2), the above-mentioned arrow is at the point situated at the right-hand side of the maximum value of the potential $U(Z,A)$. This means that also for reaction (I) induced by ^{32}S the intrinsic fusion barrier is about 1.5 MeV.

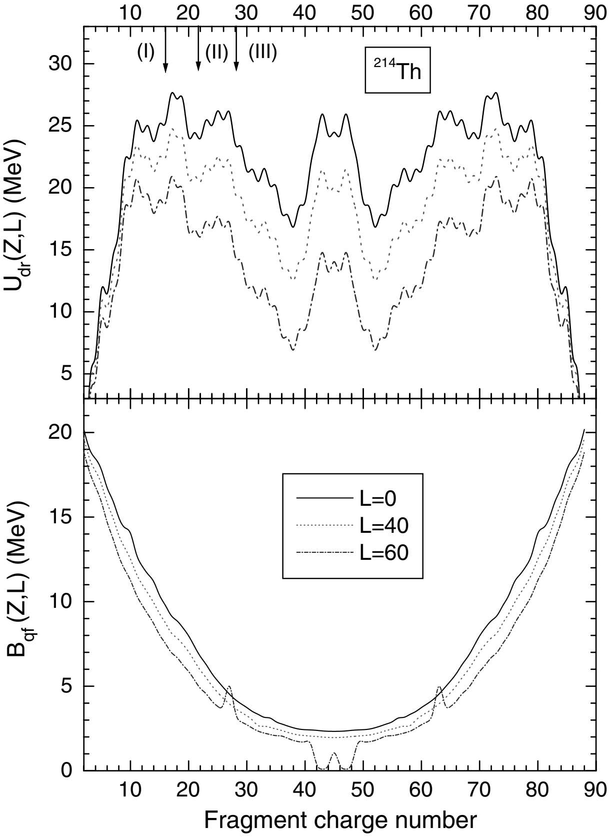

Fig. 5. The driving potential (top panel) and quasifission barrier (bottom panel) (at different orbital angular-momentum values) as a function of the fragment charge for the reactions leading to the ^{214}Th* CN.

For the other two reactions ((II) and (III)) induced by the ^{48}Ti and ^{60}Ni beams, respectively, B^*_{fus} increases and B_{qf} decreases with decreasing the η_Z parameter (see table 1). A combination of these conditions leads to an appreciable decrease in the P_{CN} value and a decrease in the fusion cross-section from reaction (I) up to reaction (III) (see fig. 4a, b, c). The driving potential is the same for all the reactions leading to the same compound nucleus. Therefore, the intrinsic fusion barriers for these reactions under discussion can be compared. The way to fusion is longer for a DNS which has a more mass-symmetric configuration.

As one can see from fig. 4 for the ^{32}S + ^{182}W (I) reaction, the fusion cross-section is comparable with the capture cross-section up to the excitation energy E^* of about 60 MeV, while at higher excitation energies the quasifission contribution exceeds the complete-fusion contribution, even in the case of the mass-asymmetric entrance channel (see fig. 4a). This is connected with the dependence of the quasifission and intrinsic fusion barriers on the orbital angular momentum (fig. 5). At higher projectile energies the dinuclear system is formed with the higher values of the orbital angular momentum. As a result, the contribution of quasifission increases due to a decrease in $B_{\rm qf}$ and an increase in $B^*_{\rm fus}$. In the case of a more massive beam and more symmetric entrance channel, as in the ^{48}Ti + ^{166}Er (II), the quasifission contribution exceeds the complete-fusion contribution also at excitation energies $E^* > 43$ MeV (fig. 4b). For the ^{60}Ni + ^{154}Sm (III) reaction, the quasifission contribution exceeds the complete-fusion contribution at all values of the beam energy (see fig. 4c).

The reaction mechanism can be studied analyzing experimental data and performing corresponding theoretical investigations. Since the experimental procedure does not allow one to register all events along the compound-nucleus de-excitation cascade, it is difficult to solve and estimate the contribution of each evaporation channel, especially at lower energies. Therefore, scarce information on the complete-fusion formation can be restored. The total cross-section of evaporation residues of xn, pxn, αxn, αpxn channels resulting from the heated and rotated compound nucleus have been calculated in the framework of the advanced statistical model [33–35]. Our calculations of the evaporation residues and the experimental total cross-section of ER presented in [45] for the ^{32}S + ^{182}W and ^{60}Ni + ^{154}Sm reactions differ by more than one order of magnitude at $E^* < 55$ MeV (see figs. 4a and c). Calculations show a hump in the αxn emission for the involved α-emitter nuclei. Indeed, the calculated results and experimental data for the excitation functions of purely xn channels are in good agreement. According to our calculations, the total xn yield is small in comparison with the yields of residues obtained after charged-particle emission, as is shown by the experimental results in [45] (see, for example, fig. 4).

Comparison of the results obtained for different reactions leading to the same compound nucleus clarifies the reaction mechanism. Theoretical analysis showed that the choice of the beam energy for the production of the compound nucleus with the same excitation energy in different reactions did not allow one to reach the same partial-fusion cross-sections at the end of the fusion stage. Since the competition between complete-fusion and quasifission processes depend on the orbital angular momentum of collision, the partial cross-sections $\sigma^{\rm fus}_\ell(E)$ of the compound-nucleus formation in different reactions are different. As a result, the evaporation residue cross-sections for different channels depend on the entrance channel. In fig. 6, these dynamical effects are shown as a function of the partial-fusion cross-sections calculated for two different reactions.

As one can see from fig. 6, the $\sigma^{\rm fus}_\ell(E_{\rm lab})$ for the (I) reaction (top panel) has a larger volume in comparison with reaction (III) (bottom panel), whereas the distribution of the partial-fusion cross-sections for reaction (III) extends to higher angular-momentum values, allowing for a larger number of geometrical configurations of reacting nuclei. The trend in the yield is connected with the $\sigma^{\rm capture}_\ell(E)$ and $P_{\rm CN}$, which determine the partial-fusion cross-sections (3).

The number of partial waves (number of angular momenta) which contribute to $\sigma^{\rm capture}_\ell(E)$ is determined by the size of the potential well in the entrance channel and its depth $B_{\rm qf}(\ell)$. The latter is one of two barriers characterizing $P_{\rm CN}$ (another is $B^*_{\rm fus}(\ell)$). It should be stressed that $B_{\rm qf}(\ell)$ and $B^*_{\rm fus}(\ell)$ depend on the orbital angular momentum: with an increase in ℓ, the quasifission barrier decreases while the intrinsic fusion barrier increases (see fig. 5). Therefore the factor $P_{\rm CN}$ (11), being a function of these barriers, $B^*_{\rm fus}$ and $B_{\rm qf}$, and determining the competition between complete fusion and quasifission, decreases with increasing ℓ at given values of the beam energy.

The appearance of wiggles in the driving potential around the fragment charges 27, 43 and the complementary charges at the angular momentum $\ell = 60\hbar$ is due to a strong dependence of the nuclear part of the nucleus-nucleus potential (eq. (A.4)) on the overlapping region of the nucleon distribution in the deformed nuclei. In turn, the overlapping region changes with increasing the impact parameter, which is a function of the angular momentum

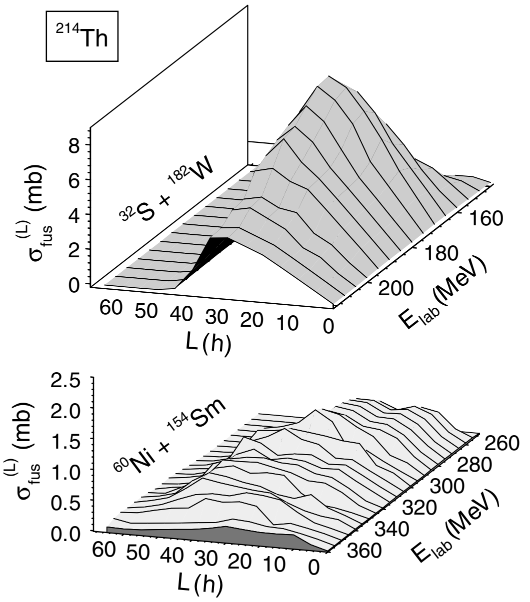

Fig. 6. The calculated distribution of the partial-fusion cross-sections for the ^{32}S + ^{182}W (top panel) and ^{60}Ni + ^{154}Sm (bottom) reactions at different beam energies $E_{\rm lab}$.

Table 2. Impact parameter values (fm) corresponding to the orbital angular momentum ($\hbar$) for two beam energies of the ^{32}S + ^{182}W and ^{60}Ni + ^{154}Sm reactions.

Reactions	^{32}S + ^{182}W		^{60}Ni + ^{154}Sm	
$E_{\rm lab}$ (MeV)	150	210	260	360
ℓ ($\hbar$)	b (fm)		b (fm)	
0	0	0	0	0
10	0.77	0.65	0.51	0.43
20	1.54	1.30	1.02	0.86
30	2.31	1.95	1.53	1.29
40	3.08	2.60	2.04	1.72
50	3.85	3.25	2.55	2.15
60	4.62	3.90	3.06	2.58

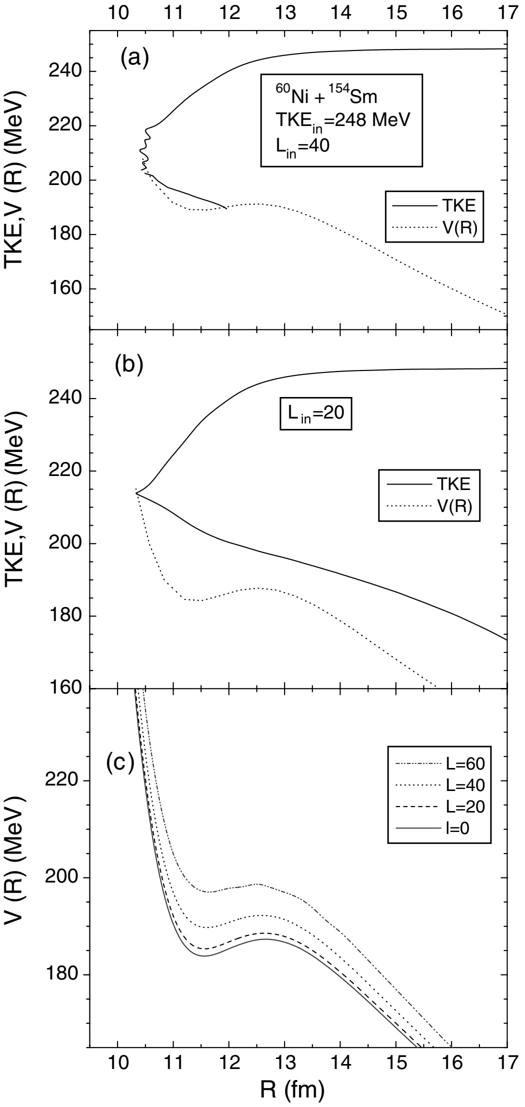

Fig. 7. Comparison of two paths *versus* R corresponding to two initial values of the orbital angular momentum of the ^{60}Ni + ^{154}Sm collision at the same value of the beam energy $E_{\text{c.m.}} = 248$ MeV (panels a and b). Capture occurs at the collision of nuclei with $\ell = 40\hbar$ (see panel a) and it does not occur at $\ell = 20\hbar$ (see panel b). The nucleus-nucleus potential $V(R)$ for different values of the orbital angular momentum is shown in panel c.

and the relative orientation of reacting nuclei in a DNS (see table 2 and fig. 14 below). These effects produce wiggles on the $B_{\text{qf}}(Z)$ curve (bottom panel of fig. 5).

The use of calculated friction coefficients leads to a gradual dissipation of kinetic and rotational energies [22]. The calculations show that at the collisions of massive nuclei, despite continuous dissipation, capture becomes impossible at beam energy values much greater than the Coulomb barrier for the low values of the orbital angular momentum (fig. 7b). The dissipation is not enough for trapping the colliding nuclei in the potential well to create a necessary condition for fusion at low values of the angular momentum, which would allow the DNS to fuse.

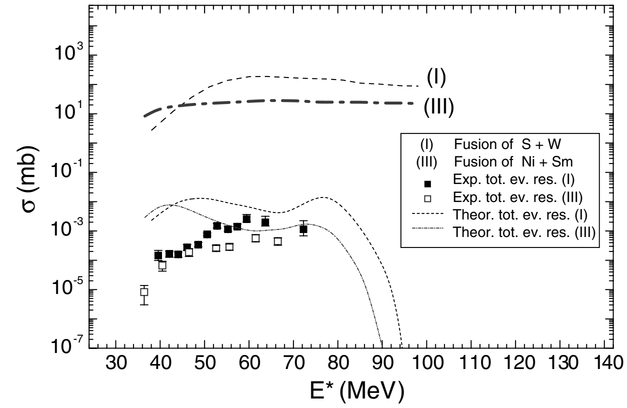

Fig. 8. Comparison of results for two very different entrance channels (^{32}S + ^{182}W and ^{60}Ni + ^{154}Sm) leading to the ^{214}Th* CN. The thick dashed line (for ^{32}S + ^{182}W) and thick dash-dotted line (for ^{60}Ni + ^{154}Sm) represent the calculated fusion cross-sections. The thin dashed line (for ^{32}S + ^{182}W) and thin dash-dotted line (for ^{60}Ni + ^{154}Sm) are the calculated total-evaporation residue cross-sections. Full squares and open squares are the experimental results [11,45] for the above-mentioned reactions induced by ^{32}S and ^{60}Ni beams, respectively.

In this case, capture is possible only for the high angular momentum (fig. 7a). The position of the potential well moves to higher energies with an increase in the orbital angular momentum. Consequently, the difference between the current value of the total kinetic energy of the relative motion and the potential energy decreases. For example, for the ^{60}Ni + ^{154}Sm reaction at higher values of the orbital angular momentum ($\ell \geq 40\hbar$ in the case presented in fig. 7), a less amount of the total kinetic energy loss is enough for the capture of the dinuclear system. The angle between the symmetry axis of the projectile (target) nucleus and the beam direction was chosen as $\alpha_1 = 30°$ ($\alpha_2 = 105°$). It should be stressed that a DNS which is formed at high values of the orbital angular momentum can exist in a molecular state, forming a super-deformed shape, or it undergoes quasifission because B^*_{fus} increases by the angular momentum of the DNS.

Therefore, the maximum of the calculated distribution of the partial-fusion cross-sections has a tendency to move to larger values of the angular momentum at beam energies well above the Coulomb barrier. It can be clearly seen in the distribution of the partial-fusion cross-sections for the two very different reactions, ^{32}S + ^{182}W and ^{60}Ni + ^{154}Sm (fig. 6).

The structure and shape of $\sigma_\ell^{\text{fus}}(E)$ for the same excited compound nucleus formed in different reactions are sensitive to dynamical effects of the entrance channel. Therefore, different entrance channels leading to the same excited compound nucleus do not generally produce the same evaporation residue cross-section, due to the dependence of the survival probability on the angular momentum of the compound nucleus. This effect is clearly shown in fig. 8, where, as an example, we compare the results for the ^{32}S + ^{182}W and ^{60}Ni + ^{154}Sm reactions.

3.2 The reactions leading to ^{221}Pa*

We present the calculation of the capture, fusion and evaporation residue excitation functions for the ^{40}Ar + ^{181}Ta reaction leading to the ^{221}Pa* compound nucleus and compare our results (see fig. 9) with the experimental data reported in refs. [46,47]. This reaction is a charge-asymmetric one ($\eta_Z = 0.61$). The large values of the above-mentioned cross-sections are related both to the small value of the intrinsic fusion barrier ($B^*_{\text{fus}} = 1.77$ MeV) and to the relatively high value of the quasifission barrier ($B_{\text{qf}} = 8.5$ MeV). These joined conditions enhance the capture and increase the ratio between the fusion and quasifission cross-sections determining the fusion factor P_{CN} to be of about 0.16 at $E^*_{\text{CN}} = 48$ MeV.

The fusion excitation function extends to the lower energies (E^* about 31 MeV); it is connected with the deformed shape of the ^{181}Ta nucleus: $\beta_2 = 0.239$ and $\beta_3 = 0.090$. Therefore, the influence of mutual orientation of nuclei in the entrance channel on the barrier is appreciable, and consequently, a large fluctuation of the entrance barrier is observed.

The evaporation residue production is strongly related to the energy dependence of partial-fusion cross-sections $\sigma_\ell^{\text{fus}}(E)$ and to the $\Gamma_{\text{n}}/\Gamma_{\text{f}}$ values at the steps of the ^{221}Pa* CN de-excitation cascade.

In fig. 9, the measured fission fragment excitation function for the ^{40}Ar + ^{181}Ta reaction from [46,47] is compared with the capture and fusion cross-sections. The huge difference between the experimental data on fission and evaporation residue cross-sections means that the fission cross-section can be considered as a complete-fusion cross-section. As in the case of the ^{40}Ar + ^{176}Hf (see fig. 2 of ref. [48]) and ^{48}Ti + ^{166}Er reactions (see fig. 4b), the capture cross-section for the ^{40}Ar + ^{181}Ta reaction (the solid line in fig. 9) is in good agreement with fragment yields up to excitation energy E^* of about 55 MeV. The difference between experimental data on fission fragments and calculations of the capture at higher excitation energies could be explained by the sizeable contribution of the deep inelastic processes because the capture cross-section decreases at $E^* > 55$ MeV (corresponding to beam energies of about $E_{\text{lab}} > 195$ MeV).

Comparing the calculated excitation function of fusion (dashed line in fig. 9) with the measured fragment yields (full squares), it is easy to conclude that in the reaction ^{40}Ar + ^{181}Ta the quasifission process exceeds the fusion-fission contribution at excitation energies $E^* > 35$ MeV. The calculated cross-sections of evaporation residues (dotted line) are in complete agreement with the measured data related to the xn emission from the compound nucleus when these fusion cross-sections are used (dashed line). It is interesting to note that in our calculation, the σ_{ER} production is 1-2 orders of magnitude lower than the complete-fusion formation (σ_{fus}) in the $E^* = 35$–60 MeV range, while the same ratio changes from 1 to 4 orders of magnitude in the same excitation energy range if the fusion cross-section is considered to be equal to the fission fragment production (full squares in fig. 9). As one can see, this last-mentioned fact is an unusual one since the fusion considerably increases while the evaporation residues strongly decrease in the $E^* = 45$–65 MeV range.

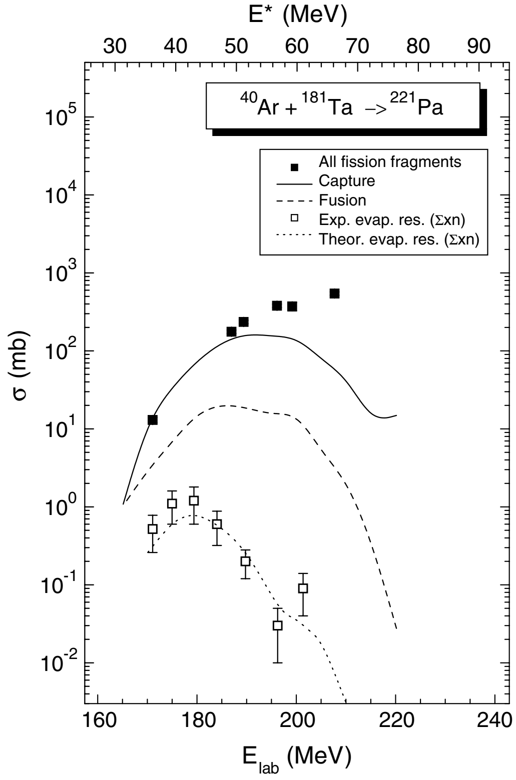

Fig. 9. The calculated capture (solid line), fusion (dashed line) and evaporation residue (dotted line) excitation functions, as well as measured excitation functions of the fission fragments (full squares) and evaporation residues (open squares) for the ^{40}Ar + ^{181}Ta reaction.

4 The formation of superheavy elements

A relevant problem in the study of the synthesis of superheavy elements in reactions with massive nuclei is finding out unambiguously the quasifission contribution in respect to the complete-fusion contribution. It is difficult enough, from experimental and theoretical points of view, to estimate the fusion cross-section from the experimental data on the reaction products with symmetric masses (with a large Δm interval). Note that the quasifission process contributes to the asymmetric-fragment production as well as into the more symmetric fragments. Moreover, the analysis of the fragment angular distribution and kinetic energy distribution of fragments also does not allow one to find out unambiguously the contribution of quasifission as compared with that of fusion-fission.

4.1 The reaction leading to ^{296}116

In accordance with the above-mentioned consideration, our calculation of the capture cross-section (solid line in fig. 10) for the ^{48}Ca + ^{248}Cm reaction leading to the

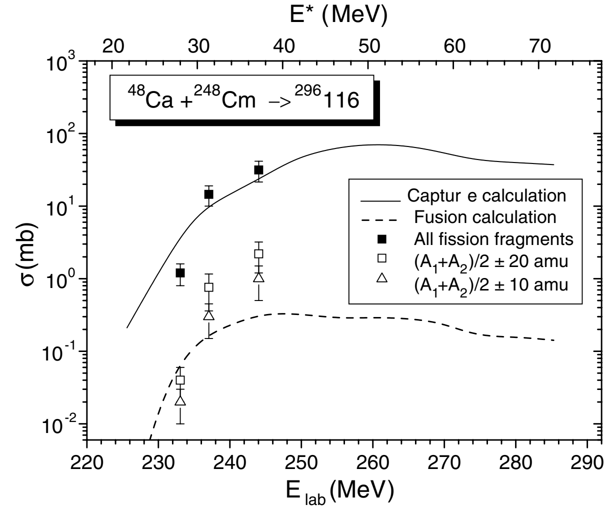

Fig. 10. The capture and fusion cross-section calculation, in comparison with the experimental data [30,49], for the ^{48}Ca + ^{248}Cm reaction leading to the ^{296}116 superheavy CN. The difference between the fusion cross-section and more symmetric fragment yield ($(A_1 + A_2)/2 \pm 10$ amu) at a higher excitation energy is related to the contribution of the quasifission process yielding more symmetric fragments.

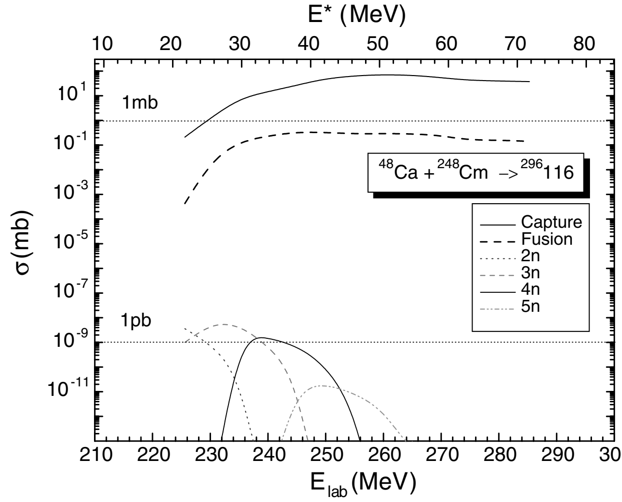

Fig. 11. The excitation functions for the evaporation residue nuclei obtained from the ^{296}116 CN after the (2–5) neutron emission in the ^{48}Ca + ^{248}Cm reaction. The figure also shows the capture and fusion cross-sections.

^{296}116 compound nucleus is in complete agreement with the experimental data [30] for the production of all fragments (full squares), while the fusion cross-section (dashed line) is not in agreement with the data (open squares) for the symmetric mass fragments ($(A_1 + A_2)/2$) when a large mass interval of ±20 amu is assumed.

Such disagreement is connected with the contribution of the quasifission process in the range of the more symmetric fragments in which the fusion-fission process also contributes. If it is assumed that the experimental fusion-fission events are in the $(A_1 + A_2)/2 \pm 10$ amu interval (almost close to the $\sqrt{(A_1 + A_2)/2}$ value), the calculated fusion cross-sections (dashed line) will be closer to the new set of the experimental data (open triangles [49] in fig. 10). Indeed, in this case there is an appreciable contribution of the quasifission process (or a contribution which cannot be neglected), in addition to the fusion-fission fragment formation. Therefore, the estimated experimental fusion cross-section, connected with the new set of the experimental events of fission fragments, still appears to be a little larger than the calculated fusion excitation function at higher excitation energies. A preliminary calculation of the mass distribution of quasifission fragments for a fixed reaction time $t_{\rm reac}$ of a DNS performed in the framework of the model developed on the basis of the dinuclear system concept [31,32], indicates that the fragments of the quasifission process also appear in the mass-symmetric region and are mixed with the fragments coming from the fusion-fission process.

In our calculation, the capture and fusion cross-sections are characterized by the intrinsic fusion barrier $B^*_{\rm fus} = 4.48$ MeV and the quasifission barrier $B_{\rm qf} = 4.12$ MeV.

In fig. 11 we also present excitation functions of the evaporation residues obtained as a result of the 2–5 neutron emission from the ^{296}116 compound nucleus. The maximum of the cross-section is several pb for the 3n emission, and it is almost 2 pb for the maximum of the 4n emission.

4.2 The reaction leading to ^{291}115

In this section we present the data on the reaction induced by the ^{48}Ca beam (even-even nucleus with a double-shell closure) on the ^{243}Am target (odd-even nucleus) leading to the ^{291}115 compound nucleus.

In our calculation we have found the intrinsic fusion barrier $B^*_{\rm fus} = 1.8$ MeV and the quasifission barrier $B_{\rm qf} = 4.2$MeV. These values lead to an appreciable ratio between fusion and quasifission. A big difference between the values of the intrinsic fusion barrier obtained for the reaction under discussion and the ^{48}Ca + ^{248}Cm reaction is related to the peculiarities of the calculated driving potentials of these reactions. For example, the maximum value of the driving potential on the way to fusion for the ^{48}Ca + ^{243}Am reaction is lower than that for the ^{48}Ca + ^{248}Cm reaction. Therefore, the compound nucleus ^{291}115 can be formed with a lower excitation energy as compared with ^{296}116.

In fig. 12 we present the capture and fusion cross-sections as well as the excitation functions of the evaporation residues after the emission of 2–5 neutrons from the ^{291}115 excited compound nucleus. As one can see, the fusion cross-section is about 1–2 mb for a wider beam energy range, the maximum for the $\mathrm{ER}_{3\mathrm{n}}$ is about 8 pb at $E^* = 26$ MeV and the maximum for $\mathrm{ER}_{4\mathrm{n}}$ is about 1 pb at $E^* = 35$ MeV.

The present reaction, forming the ^{291}115 compound nucleus, appears to have a slightly higher yield of residues

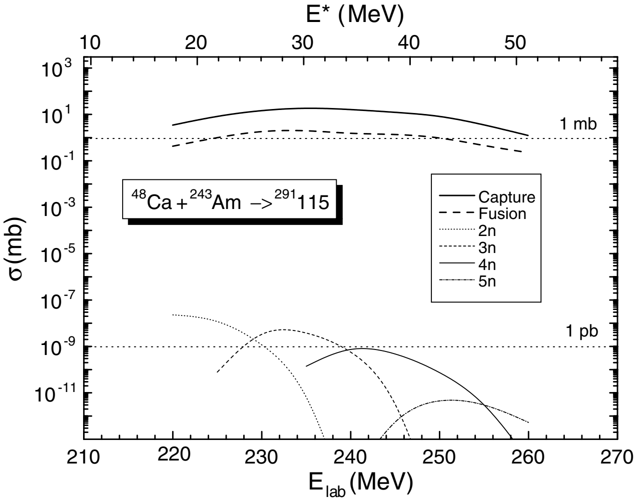

Fig. 12. The excitation functions for the evaporation residue nuclei obtained from the ^{291}115 CN after the (2–5) neutron emission in the ^{48}Ca + ^{243}Am reaction. The figure also shows the capture and fusion cross-sections.

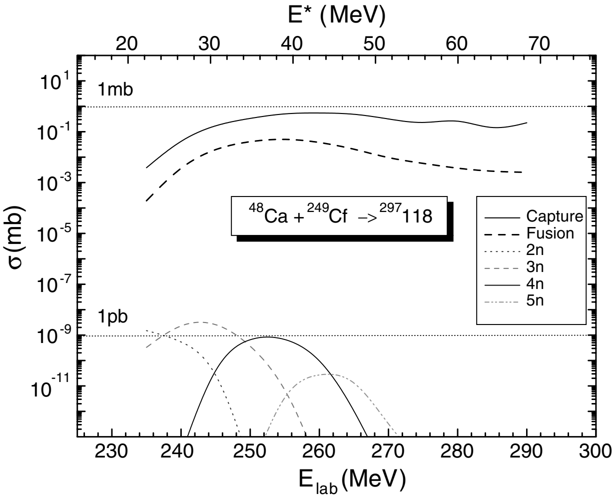

Fig. 13. The same as in fig. 11 but for the ^{297}118 superheavy CN obtained in the ^{48}Ca + ^{249}Cf reaction. The capture, fusion and evaporate residue cross-sections are lower than those obtained for the ^{296}116 CN in the ^{48}Ca + ^{248}Cm reaction.

than reactions leading to $Z_{\mathrm{CN}} = 114$ [50] and 116. This result is related to the very low value of the intrinsic fusion barrier $B^*_{\mathrm{fus}} = 1.8$ MeV and to the relatively high value of the survival probability against fission of the excited compound nucleus due to a substantial shell correction in the fission barrier.

4.3 The reaction leading to ^{297}118

We also present our calculations for the ^{48}Ca + ^{249}Cf reaction, leading to the ^{297}118 compound nucleus, aiming at the evaluation of the fusion cross-section and the excitation functions for the evaporation residue nuclei obtained as a result of the x (2–5) neutron emission from the compound nucleus. For this reaction, we obtained the intrinsic fusion barrier $B^*_{\mathrm{fus}} = 9$ MeV and the quasifission barrier $B_{\mathrm{qf}} = 4.5$ MeV.

Figure 13 shows the capture cross-section (lower than 1 mb) and the fusion cross-section (with a maximum value of about $50\,\mu$b) *versus* the beam energy. For the evaporation residue cross-section, we found the maximum values of about 3.5 pb for the 3n channel, and of about 0.8-0.9 pb for the 4n channel.

Comparing the results of the ^{48}Ca + ^{248}Cm, ^{249}Cf reactions leading to the ^{296}116 and ^{297}118 compound nuclei, respectively, one can make a conclusion that the complete fusion decreases, as does the evaporation residue nuclei ($\mathrm{ER}_{3\mathrm{n},4\mathrm{n}}$) in the case of the ^{297}118 nucleus formation.

5 Conclusions

The role of the entrance channel in fusion-fission reactions was studied aiming at the explanation of the difference between the experimental data for the ^{32}S + ^{182}W, ^{48}Ti + ^{166}Er, and ^{60}Ni + ^{154}Sm reactions leading to the ^{214}Th* CN. A combined dynamical and statistical model based on the DNS approach was used to estimate the excitation functions of quasifission, fusion, and formation of evaporation residues in reactions with massive nuclei. The capture stage was calculated by numerical solution of a classical equation of motion for a relative distance between nuclei and the orbital angular momentum of collision. The nucleus-nucleus potential is calculated taking into account possible mutual orientations of deformed nuclei. The coefficients of radial and tangential friction are calculated simultaneously by the estimation of nucleon exchange and particle-hole excitations in nuclei, *i.e.* microscopically. The maximum value of ℓ leading to capture for a given beam energy and initial orientation of nuclei is calculated in the framework of this model. Then the fusion stage is calculated within the statistical approach using the excitation energy of a dinuclear system, level densities at intrinsic fusion and quasifission barriers. The fusion excitation functions thus calculated were used for the estimation of the survival probability of the formed compound nucleus against fission in the framework of the advanced statistical model for the de-excitation cascade. The fission barriers which were used in this model were obtained from the rotating droplet model (angular-momentum dependent) as parameterized by Sierk [40]. They allow for the angular momentum and temperature fade-out of the shell corrections.

The results of the calculations obtained in the framework of the DNS concept and advanced statistical model for evaporation residue cross-sections for the sum of the xn-channel contributions have been compared with the experimental data obtained in the ^{32}S + ^{182}W, ^{48}Ti + ^{166}Er, and ^{60}Ni + ^{154}Sm reactions [11,45] leading to the ^{214}Th* CN.

For the ^{32}S + ^{182}W reaction, the competition between complete-fusion and quasifission processes begins at beam energies corresponding to $E^* = 60$ MeV, whereas for the reactions with more massive nuclei this occurs at beam energies corresponding to $E^* > 43$ MeV in the case of ^{48}Ti + ^{166}Er, or to $E^* > 30$ MeV for ^{60}Ni + ^{154}Sm.

The big difference between the values of the $\sigma_{\rm ER}/\sigma_{\rm fus}$ ratio calculated for the ^{40}Ar + ^{181}Ta reaction in the present work and that extracted from experimental data in the excitation energy range of 35–60 MeV is explained by the overestimation of the cross-section of the fusion-fission fragments due to a sizeable contribution of the quasifission process into the fragment yield. Having analyzed the ^{48}Ca + ^{248}Cm reaction, we note that the quasifission process also contributes to the symmetric-fragment formation at higher excitation energies.

As for the synthesis of superheavy elements, the ^{48}Ca + ^{243}Am reaction yields appreciable values of the evaporation residue cross-section, while for the other two investigated reactions leading to $Z = 116$, 118, the respective cross-sections (capture, fusion and evaporation residue nuclei) decrease.

In the calculations of the evaporation residue excitation function, the choice of suitable parameters allows a description of experimental data; however the peculiarity of the reaction mechanism of projectile-target pairs with different mass-asymmetries still remains unclear. It is difficult to measure directly the fusion cross-section since it is difficult to establish the origin of the fusion-fission reaction fragments unambiguously.

Due to the fact that the nuclear shell effect and the shape of colliding nuclei are taken into account in the calculation of the competition between complete-fusion and quasifission processes, the mechanism of the fusion-fission process can be analyzed. Thus, the DNS concept reveals the reason for the strong decrease in the fusion cross-section for a massive system or for a symmetric entrance channel. The smallness of the evaporation residue cross-sections for the ^{60}Ni + ^{154}Sm reaction in comparison with that for the other ^{32}S + ^{182}W and ^{48}Ti + ^{166}Er reactions leading to the same ^{214}Th* is explained by the effect of quasifission. We have shown that the competition of quasifission with complete fusion increases by the intrinsic fusion barrier.

This work was performed partially under a financial support of the RFBR (Grant No. 99-02-16447) and INTAS (Grant No. 991-1344). The authors (A.I.M and A.K.N.) are grateful to the STCU Uzb-45 for the support. A.K.N. would like to express his gratitude for the warm hospitality offered to him during his stay at the University of Messina (Italy). A.K.N. and U.T.Y. are also grateful to the Fondazione Bonino-Pulejo (FBP) of Messina for the support received in the collaboration with the Messina group.

Appendix A. Nucleus-nucleus potential and kinetic coefficients

The nucleus-nucleus potential is calculated as follows:

$$V_0(R) = V_{\rm C}(R) + V_{\rm nucl}(R) + V_{\rm rot}(R), \qquad \text{(A.1)}$$

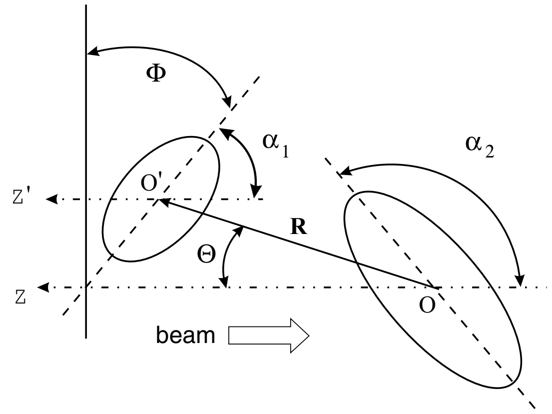

Fig. 14. The coordinate systems and angles which were used for the description of the initial orientations of projectile and target nuclei. The beam direction is opposite to OZ.

where $V_{\rm C}(R)$, $V_{\rm nucl}(R)$, and $V_{\rm rot}(R)$ are the Coulomb, nuclear, and rotational potentials, respectively. The nuclear shape is important in the calculation of the Coulomb and nuclear interactions between colliding nuclei. Thus, the Coulomb interaction of deformed nuclei can be calculated according to the following expression taken from [51]:

$$\begin{aligned} V_{\rm C}(R) = {} & \frac{Z_1 Z_2}{R} e^2 \\ & + \frac{Z_1 Z_2}{R^3} e^2 \left\{ \left(\frac{9}{20\pi}\right)^{1/2} \sum_{i=1}^{2} R_{0i}^2 \beta_2^{(i)} \mathcal{P}_2(\cos\alpha_i') \right. \\ & \left. + \frac{3}{7\pi} \sum_{i=1}^{2} R_{0i}^2 \left[\beta_2^{(i)} \mathcal{P}_2(\cos\alpha_i')\right]^2 \right\}, \end{aligned} \qquad \text{(A.2)}$$

where $\alpha_1' = \alpha_1 + \Theta$, $\alpha_2' = \pi - (\alpha_2 + \Theta)$, $\sin\Theta = |\mathbf{L}|/(\mu \dot{R} R)$; Z_i, $\beta_2^{(i)}$, and α_i' are the atomic number (for each fragment), the quadrupole deformation parameter, and the angle (see fig. 14) between the line connecting the centers of masses of the nuclei and the symmetry axis of the fragment $i (i = 1, 2)$, respectively. Here, $R_{0i} = r_0 A_i^{1/3}, r_0 = 1.18$ fm and $\mathcal{P}_2(\cos\alpha_i')$ is the second term of the second type of Legendre polynomial.

The nuclear part of the nucleus-nucleus potential is calculated using the folding procedure between the effective nucleon-nucleon forces $f_{\rm eff}[\rho(x)]$ suggested by Migdal [52] and the nucleon density of the projectile and target nuclei, $\rho_1^{(0)}$ (B.5) and $\rho_2^{(0)}$ (B.1), respectively:

$$V_{\rm nucl}(R) = \int \rho_1^{(0)}(\mathbf{r} - \mathbf{r}_1) f_{\rm eff}[\rho] \rho_2^{(0)}(\mathbf{r} - \mathbf{r}_2) {\rm d}^3\mathbf{r}\,, \qquad \text{(A.3)}$$

$$f_{\rm eff}[\rho] = 300 \left(f_{\rm in} + (f_{\rm ex} - f_{\rm in}) \frac{\rho(0) - \rho(r)}{\rho(0)} \right). \qquad \text{(A.4)}$$

Here $f_{\rm in} = 0.09$, $f_{\rm ex} = -2.59$ are the constants of the effective nucleon-nucleon interaction; $\rho = \rho_1^{(0)} + \rho_2^{(0)}$ (details are in appendix B).

Expressions for the friction coefficients

$$\gamma_R(R(t)) = \sum_{i,i'} \left|\frac{\partial V_{ii'}(R(t))}{\partial R}\right|^2 B^{(1)}_{ii'}(t), \tag{A.5}$$

$$\gamma_\theta(R(t)) = \frac{1}{R^2} \sum_{i,i'} \left|\frac{\partial V_{ii'}(R(t))}{\partial \theta}\right|^2 B^{(1)}_{ii'}(t), \tag{A.6}$$

and the dynamic contribution to the nucleus-nucleus potential

$$\delta V(R(t)) = \sum_{i,i'} \left|\frac{\partial V_{ii'}(R(t))}{\partial R}\right|^2 B^{(0)}_{ii'}(t), \tag{A.7}$$

were obtained in [22] by estimating the evolution of the coupling term between relative motion of nuclei and nucleon motion inside nuclei; $B^{(0)}_{ii'}(t)$ is given by eq. (A.9).

The dynamic correction of the reduced mass $\delta\mu(R(t))$ is calculated using the expression

$$\begin{aligned}\delta\mu(R(t)) = {} & \sum_{i,i'} \left|\frac{\partial V_{ii'}(R(t))}{\partial R}\right|^2 B^{(2)}_{ii'}(t) \\ & -\mu_0 \frac{2}{A_{\mathrm{tot}}} \int \frac{\rho_1^{(0)}(r-r_1)\rho_2^{(0)}(r-r_2)}{\rho_1^{(0)}(r-r_1)+\rho_2^{(0)}(r-r_2)} \mathrm{d}^3 r,\end{aligned} \tag{A.8}$$

where $B^{(2)}_{ii'}(t)$ is given by

$$\begin{aligned}B^{(n)}_{ik}(t) = {} & \frac{2}{\hbar} \int_0^t \mathrm{d}t' (t-t')^n \exp\left(\frac{t'-t}{\tau_{ik}}\right) \\ & \times \sin\left[\omega_{ik}\left(R(t')\right)(t-t')\right]\left[\tilde{n}_k(t') - \tilde{n}_i(t')\right],\end{aligned} \tag{A.9}$$

$$\hbar\omega_{ik} = \varepsilon_i + \Lambda_{ii} - \varepsilon_k - \Lambda_{kk}\,. \tag{A.10}$$

Here $\tilde{n}_i$ is the diagonal matrix element of the density matrix which is calculated according to the model presented elsewhere [22,53]; $\tau_{ik} = \tau_i\tau_k/(\tau_i+\tau_k)$; τ_i is the lifetime of the quasiparticle excitations in the single-particle state i of the nucleus. It determines the damping of single-particle motion. τ_i is calculated using the results of the quantum liquid theory [54] and the effective nucleon-nucleon forces from [52]:

$$\begin{aligned}\frac{1}{\tau_i^{(\alpha)}} = {} & \frac{\sqrt{2}\pi}{32\hbar\varepsilon^{(\alpha)}_{\mathrm{F}_K}} \left[(f_K - g)^2 + \frac{1}{2}(f_K + g)^2\right] \\ & \times \left[\left(\pi T_K\right)^2 + \left(\tilde{\varepsilon}_i - \lambda_K^{(\alpha)}\right)^2\right] \\ & \times \left[1 + \exp\left(\frac{\lambda_K^{(\alpha)} - \tilde{\varepsilon}_i}{T_K}\right)\right]^{-1},\end{aligned} \tag{A.11}$$

where

$$T_K(t) = 3.46\sqrt{\frac{E^*_K(t)}{\langle A_K(t)\rangle}} \tag{A.12}$$

is the effective temperature determined by the amount of intrinsic excitation energy $E^*_K = E^{*(Z)}_K + E^{*(N)}_K$ and by the mass number $\langle A_K(t)\rangle$ (with $\langle A_K(t)\rangle = \langle Z_K(t)\rangle + \langle N_K(t)\rangle$). In addition, $\lambda_K^{(\alpha)}(t)$ and $E^{*(\alpha)}_K(t)$ are the chemical potential and intrinsic excitation energies for the proton ($\alpha = Z$) and neutron ($\alpha = N$) subsystems of the nucleus $K (K = 1(\text{projectile}), 2(\text{target}))$, respectively. Furthermore, the finite size of the nuclei and the difference between the numbers of neutrons and protons makes it necessary to use the following expressions for the Fermi energies [52]:

$$\begin{aligned}\varepsilon^{(Z)}_{\mathrm{F}_K} &= \varepsilon_{\mathrm{F}}\left[1 - \frac{2}{3}(1 + 2f'_K)\frac{\langle N_K\rangle - \langle Z_K\rangle}{\langle A_K\rangle}\right], \\ \varepsilon^{(N)}_{\mathrm{F}_K} &= \varepsilon_{\mathrm{F}}\left[1 + \frac{2}{3}(1 + 2f'_K)\frac{\langle N_K\rangle - \langle Z_K\rangle}{\langle A_K\rangle}\right],\end{aligned} \tag{A.13}$$

where $\varepsilon_{\mathrm{F}} = 37$ MeV,

$$\begin{aligned}f_K &= f_{\mathrm{in}} - \frac{2}{\langle A_K\rangle^{1/3}}(f_{\mathrm{in}} - f_{\mathrm{ex}}), \\ f'_K &= f'_{\mathrm{in}} - \frac{2}{\langle A_K\rangle^{1/3}}(f'_{\mathrm{in}} - f'_{\mathrm{ex}})\end{aligned} \tag{A.14}$$

and $f_{\mathrm{in}} = 0.09$, $f'_{\mathrm{in}} = 0.42$, $f_{\mathrm{ex}} = -2.59$, $f'_{\mathrm{ex}} = 0.54$, $g = 0.7$ are the constants of the effective nucleon-nucleon interaction.

Finally, the rotational potential is

$$V_{\mathrm{rot}}(R) = \hbar^2 \frac{l(l+1)}{2\mu R^2}. \tag{A.15}$$

The moment of inertia of the axial deformed nucleus for the rotation around the axis perpendicular to its axial symmetry is calculated by the expression

$$J_i = \frac{M_i}{5R_{i(\parallel)}} R_{i(\perp)}\left(R^2_{i(\perp)} + R^2_{i(\parallel)}\right) \qquad (i = 1, 2)\,, \tag{A.16}$$

where M_i is the mass of the nucleus; $R_\perp(\beta_2)$ and $R_\parallel(\beta_2)$ are the nucleus axes which are perpendicular and parallel to the symmetry axis, respectively,

$$\begin{aligned}R_\perp(\beta_2) &= R_0\left[1 + \beta_2 Y_{20}\left(\frac{\pi}{2}\right)\right], \\ R_\parallel(\beta_2) &= R_0\left[1 + \beta_2 Y_{20}(0)\right].\end{aligned}$$

Here R_0 is the spherical equivalent radius. The moment of inertia of a DNS is calculated by the rigid-body approximation

$$J_R(\alpha_1, \alpha_2; R) = \mu R^2(\alpha_1, \alpha_2) + J_1 + J_2\,, \tag{A.17}$$

where $R(\alpha_1, \alpha_2)$ is the distance between the centers of nuclei at their given mutual orientations.

Appendix B. Space distribution of nucleon density

The angles between the symmetry axis of the projectile and target nucleus and the beam direction are α_1 and α_2, respectively (fig. 14). The spherical coordinate system O

with the vector r, angles θ and ϕ is placed at the mass center of the target nucleus and the Oz axis is directed opposite to the beam. In this coordinate system, the direction of the vector $\mathbf{R}$ connecting the mass centers of the interacting nuclei has angles Θ and Φ: $\mathbf{r}_1 = \mathbf{R}$ and $\mathbf{r}_2 = 0$. The coordinate system is chosen in such a way that the planes, in which the symmetry axes of nuclei are located, cross the Oz line and form the angle Φ. For head-on collisions $\Theta = 0$ and $\Phi = \phi$.

The nucleon distribution functions of interacting nuclei in the integrand (A.3) can be expressed using these variables in the same coordinate system O. The shape of the dinuclear system nuclei changes with the evolution of the mass asymmetry degrees of freedom: $\beta_2 = \beta_2(Z, A)$ and $\beta_3 = \beta_3(Z, A)$. In order to calculate the potential energy surface as a function of the charge number, we use the values of $\beta_2^{(2^+)}$ from [55] and the values of $\beta_3^{(3^-)}$ from [56]. In the O system the symmetry axis of the target nucleus is turned around the α_2 angle, so its nucleon distribution function is as follows:

$$\rho_2^{(0)}(r) = \rho_0 \left\{ 1 + \exp\left[\frac{r - \tilde{R}_2(\beta_2^{(2)}, \beta_3^{(2)}; \theta_2')}{a} \right] \right\}^{-1},$$

$$\tilde{R}_2(\beta_2^{(2)}, \beta_3^{(2)}; \theta_2') = R_0^{(2)} \left(1 + \beta_2^{(2)} Y_{20}(\theta_2') + \beta_3^{(2)} Y_{30}(\theta_2') \right), \tag{B.1}$$

where $\rho_0 = 0.17\,\mathrm{fm}^{-3}$, $a_0 = 0.54$ fm,

$$\cos\theta_2' = \cos\theta \cos(\pi - \alpha_2) + \sin\theta \sin(\pi - \alpha_2) \cos\phi\,. \tag{B.2}$$

The mass center of the projectile nucleus is shifted to the end of the vector R and its symmetry axis is turned by the angle $\pi - \alpha_1$. According to the transformation formulae of the parallel transfer of vectors the variables of the transferred system O' are as follows:

$$\begin{aligned} r'^2 &= r^2 + R^2 - 2rR\cos(\omega_{12}), \\ \cos(\omega_{12}) &= \cos\theta\cos\Theta + \sin\theta\sin\Theta\cos(\phi - \Phi), \\ \cos\theta_1' &= \frac{(r\cos\theta - R\cos\Theta)}{r'}, \\ \cos\phi_1' &= (1 + \tan^2\phi_1')^{-1/2}, \\ \tan\phi_1' &= \frac{r\sin\phi\sin\theta - R\sin\Theta\sin\Phi}{r\cos\phi\sin\theta - R\sin\Theta\cos\Phi}\,. \end{aligned} \tag{B.3}$$

In the coordinate system O', the deviation of the symmetry axis of projectile nuclei relative to the $O'z'$ axis is determined by the angle

$$\cos\theta_1'' = \cos\theta_1' \cos(\pi - \alpha_1) + \sin\theta_1' \cos\phi_1'. \tag{B.4}$$

Now the nucleon distribution function of the projectile-nucleus looks like this

$$\rho_1^{(0)}(r') = \rho_0 \left\{ 1 + \exp\left[\frac{r' - \tilde{R}_1(\beta_2^{(1)}, \beta_3^{(1)}; \theta_1')}{a} \right] \right\}^{-1},$$

$$\tilde{R}_1(\beta_2^{(1)}, \beta_3^{(1)}; \theta_1') = R_0^{(1)} \left(1 + \beta_2^{(1)} Y_{20}(\theta_1') + \beta_3^{(1)} Y_{30}(\theta_1') \right). \tag{B.5}$$

The nuclear part of the nucleus-nucleus potential was calculated by (A.3) using the folding procedure of the effective nucleon-nucleon forces by Migdal [52] with the nucleon distribution functions (B.1) and (B.5) of the interacting nuclei.

References

1. F. Hanappe, M. Lefort, C. Ngo, J. Peter, B. Tamain, Phys. Rev. Lett. **32**, 738 (1974).
2. M. Lefort, Phys. Rev. C **12**, 686 (1975).
3. H.C. Britt, B.H. Erkkila, R.H. Stokes, H.H. Gutbrod, F.Plasil, R.L. Ferguson, M. Blann, Phys. Rev. C **13**, 1483 (1976).
4. B.B. Back, R.R. Betts, K. Cassidy, B.G. Glagola, J.E. Gindler, L.E. Glendenin, B.D. Wilkins, Phys. Rev. Lett. **50**, 818 (1983).
5. B.B. Back, Phys. Rev. C **31**, 2104 (1985).
6. J. Tõke *et al.*, Nucl. Phys. A **440**, 327 (1985).
7. J. Tõke *et al.*, Phys. Lett. B **142**, 258 (1984).
8. W.Q. Shen *et al.*, Europhys. Lett. **1**, 113 (1986).
9. W.Q. Shen *et al.*, Phys. Rev. C **36**, 115 (1987).
10. B.B. Back *et al.*, Phys. Rev. C **32**, 195 (1985).
11. B.B. Back *et al.*, Phys. Rev. C **53**, 1734 (1996).
12. N.V. Antonenko, E.A. Cherepanov, A.K. Nasirov, V.P. Permjakov, V.V. Volkov, Phys. Lett. B **319**, 425 (1993); Phys. Rev. C **51**, 2635 (1995).
13. G. Giardina, F. Hanappe, A.I. Muminov, A.K. Nasirov, L. Stuttgé, Nucl. Phys. A **671**, 165 (2000).
14. G. Giardina, S. Hofmann, A.I. Muminov, A.K. Nasirov, Eur. Phys. J. A **8**, 205 (2000).
15. W.J. Swiatecki, Phys. Scr. **24**, 113 (1981); Nucl. Phys. A **376**, 275 (1982).
16. P. Fröbrich, Phys. Rep. **116**, 337 (1984); Phys. Lett. B **215**, 36 (1988).
17. K.T.R. Davies, A.J. Sierk, J.R. Nix, Phys. Rev. C **28**, 679 (1983).
18. J.P. Blocki, H. Feldmeier, W.J. Swiatecki, Nucl. Phys. A **459**, 145 (1986).
19. G. Audi, A.H. Wapstra, Nucl. Phys. A **595**, 509 (1995).
20. P. Möller, J.R. Nix, At. Data Nucl. Data Tables **39**, 213 (1988).
21. G.G. Adamian, R.V. Jolos, A.K. Nasirov, Z. Phys. A **347**, 203 (1994).
22. G.G. Adamian, R.V. Jolos, A.I. Muminov, A.K. Nasirov, Phys. Rev. C **56**, 373 (1997).
23. J. Velkovska, C.R. Morton, R.L. McGrath, P. Chung, I. Diószegi, Phys. Rev. C **59**, 1506 (1999).
24. D.J. Hinde, D. Hilsher, H. Rossner, B. Gebauer, M. Lehmann, M. Wilpert, Phys. Rev. C **45**, 1229 (1992).
25. K. Siwek-Wilczynska, J. Wilczynski, R.H. Siemssen, H.W. Wilschut, Phys. Rev. C **51**, 2054 (1995).
26. G.G. Adamian, G. Giardina, A.K. Nasirov, in *Proceedings of the International Workshop on Nuclear Fission Physics, Obninsk, 1998*, edited by V. Dolzhenko, V. Zamarenova, Yu. Kulinova (Institute fo Power Physics and Power Engineering, Obninsk, 2000) pp. 106-116.
27. G.G. Adamian, N.V. Antonenko, W. Scheid, Nucl. Phys. A **618**, 176 (1997).
28. R. Butsch, D.J. Hofman, C.P. Montoya, P. Paul, M. Thoennessen, Phys. Rev. C **44**, 1515 (1991).

29. A.A. Bogatchev *et al.*, *Proceedings of the International Conference on Nuclear Physics at Border Lines May 21-24, 2001, Lipari (Messina), Italy*, edited by G. Fazio, G. Giardina, F. Hanappe, G. Imme, N. Rowley (World Scientific, Singapore, 2002) pp. 56-59.
30. M.G. Itkis *et al.*, *Proceedings of the International Conference on Nuclear Physics at Border Lines, May 21-24, 2001, Lipari (Messina), Italy*, edited by G. Fazio, G. Giardina, F. Hanappe, G. Imme, N. Rowley (World Scientific, Singapore, 2002) pp. 146-156.
31. R.V. Dzholos, S.M. Lukyanov,A.K. Nasirov,V.P. Permyakov, V.S. Salamatin, G.G. Chubaryan, Sov. J. Nucl. Phys. **50**, 382 (1989).
32. G. Fazio *et al.*, *Proceedings of the International Symposium on New Projects and Lines of Research in Nuclear Physics, October 24-26, 2002, Messina, Italy*, edited by G. Fazio, F. Hanappe (World Scientific, Singapore, 2003) pp. 258-271.
33. A. D'Arrigo, G. Giardina, M. Herman, A. Taccone, Phys. Rev. C **46**, 1437 (1992).
34. A. D'Arrigo, G. Giardina, M. Herman, A.V. Ignatyuk, A. Taccone, J. Phys. G **20**, 365 (1994).
35. R.N. Sagaidak, V.I Chepigin, A.P. Kabachenko, J. Roháč, Yu.Ts. Oganessian, A.G. Popeko, A.V. Yeremin, A. D'Arrigo, G. Fazio, G. Giardina, M. Herman, R. Ruggeri, R. Sturiale, J. Phys. G **24**, 611 (1998).
36. O. Bohr, B. Mottelson, *Nuclear Structure*, Vols. **I** and **II** (Benjamin, New York, Amsterdam, 1975).
37. S.E. Vigdor, H.J. Karwowski, Phys. Rev. C **26**, 1068 (1982).
38. A.V. Ignatyuk, G.N. Smirenkin, A.S. Tishin, Yad. Fiz., **21**, 485 (1975) (Sov. J. Nucl. Phys. **21**, 255 (1975)).
39. A.V. Ignatyuk, K.K. Istekov, G.N. Smirenkin, Sov. J. Nucl. Phys. **29**, 450 (1979).
40. A.J. Sierk, Phys. Rev. C **33**, 2039 (1986).
41. P. Grange, H.A. Weidenmüller, Phys. Lett. B **96**, 26 (1980).
42. E.M. Rastopchin, S.I. Mulgin, U.V. Ostapenko, V.V. Pashkeevich, M.I. Svirin, G.N. Smirenkin, Sov. J. Nucl. Phys. **53**, 741 (1991).
43. H.A. Kramers, Physica **7**, 284 (1940).
44. C. Bhattacharya, S. Bhattacharya, K. Krishan, Phys. Rev. C **53**, 1012 (1996).
45. S. Mitsuoka, H. Ikezoe, K. Nishio, J. Lu, Phys. Rev. C **62**, 054603 (2000).
46. D. Vermeulen, H.-G. Clerc, C.-C. Sahm, K.-H. Schmidt, J.G. Keller, G. Münzenberg, W. Reisdorf, Z. Phys. A **318**, 157 (1984).
47. H.-G. Clerc, J.G. Keller, C.-C. Sahm, K.-H. Schmidt, H. Schulte, D. Vermeulen, Nucl. Phys. A **419**, 571 (1984).
48. G. Fazio *et al.*, *Proceedings of the VII International School Seminar on Heavy Ion Physics, May 27-June 1, 2002 Dubna, Russia*, Phys. At. Nucl. **66**, 1071 (2003).
49. E. Kozulin, private communication.
50. Yu.Ts. Oganessian *et al.*, Nature **400**, 242 (1999).
51. C.Y. Wong, Phys. Rev. Lett. **31**, 766 (1973).
52. A.B. Migdal, *Theory of the Finite Fermi-Systems and Properties of Atomic Nuclei* (Moscow, Nauka, 1983).
53. G.G. Adamian, A.K. Nasirov, N.V. Antonenko, R.V. Jolos, Phys. Part. Nucl. **25**, 583 (1994).
54. D. Pines, P. Noziéres, *Theory of Quantum Liquids* (Benjamin, New York, 1966).
55. S. Raman, C.H. Malarkey, W.T. Milner, C.W. Nestor jr., P.H. Stelson, At. Data Nucl. Data Tables **36**, 1 (1987).
56. R.H. Spear, At. Data Nucl. Data Tables **42**, 55 (1989).